Population of anatomically variable 4D XCAT adult phantoms for imaging research and optimization

W. P. Segars,[a] Jason Bond, Jack Frush, Sylvia Hon, and Chris Eckersley
Carl E. Ravin Advanced Imaging Laboratories, Department of Radiology, The Duke University Medical Center, Durham, North Carolina 27705

Cameron H. Williams
Department of Radiology, The Duke University Medical Center, Durham, North Carolina 27710

Jianqiao Feng, Daniel J. Tward, Tilak J. T. Ratnanather, and M. I. Miller
Center for Imaging Science, the Johns Hopkins University, Baltimore, Maryland 21218

D. Frush
Department of Radiology, The Duke University Medical Center, Durham, North Carolina 27710

E. Samei
Carl E. Ravin Advanced Imaging Laboratories, Department of Radiology, The Duke University Medical Center, Durham, North Carolina 27705

(Received 2 November 2012; revised 25 January 2013; accepted for publication 15 February 2013; published 15 March 2013)

Purpose: The authors previously developed the 4D extended cardiac-torso (XCAT) phantom for multimodality imaging research. The XCAT consisted of highly detailed whole-body models for the standard male and female adult, including the cardiac and respiratory motions. In this work, the authors extend the XCAT beyond these reference anatomies by developing a series of anatomically variable 4D XCAT adult phantoms for imaging research, the first library of 4D computational phantoms.
Methods: The initial anatomy of each phantom was based on chest–abdomen–pelvis computed tomography data from normal patients obtained from the Duke University database. The major organs and structures for each phantom were segmented from the corresponding data and defined using nonuniform rational B-spline surfaces. To complete the body, the authors manually added on the head, arms, and legs using the original XCAT adult male and female anatomies. The structures were scaled to best match the age and anatomy of the patient. A multichannel large deformation diffeomorphic metric mapping algorithm was then used to calculate the transform from the template XCAT phantom (male or female) to the target patient model. The transform was applied to the template XCAT to fill in any unsegmented structures within the target phantom and to implement the 4D cardiac and respiratory models in the new anatomy. Each new phantom was refined by checking for anatomical accuracy via inspection of the models.
Results: Using these methods, the authors created a series of computerized phantoms with thousands of anatomical structures and modeling cardiac and respiratory motions. The database consists of 58 (35 male and 23 female) anatomically variable phantoms in total. Like the original XCAT, these phantoms can be combined with existing simulation packages to simulate realistic imaging data. Each new phantom contains parameterized models for the anatomy and the cardiac and respiratory motions and can, therefore, serve as a jumping point from which to create an unlimited number of 3D and 4D variations for imaging research.
Conclusions: A population of phantoms that includes a range of anatomical variations representative of the public at large is needed to more closely mimic a clinical study or trial. The series of anatomically variable phantoms developed in this work provide a valuable resource for investigating 3D and 4D imaging devices and the effects of anatomy and motion in imaging. Combined with Monte Carlo simulation programs, the phantoms also provide a valuable tool to investigate patient-specific dose and image quality, and optimization for adults undergoing imaging procedures. [http://dx.doi.org/10.1118/1.4794178]

Key words: medical imaging simulation, computer phantom, SPECT, PET, CT, MRI, ultrasound

I. INTRODUCTION

Computerized phantoms and simulation techniques are playing an important role in medical imaging research. They give researchers the ability to perform clinical experiments entirely on the computer. Computer-based models of the image formation process simulate the imaging system while the phantoms simulate the patients. With this combination, imaging data can be generated and reconstructed under a limitless possibility of scanning conditions and parameters. The phantoms can be

imaged repeatedly with no worries of radiation exposure so experiments that would otherwise be impossible to do with live subjects can be performed; such an advantage is especially important in computed tomography (CT) research. The entire anatomy of the phantoms is known so there is a "gold standard" or "truth" from which to quantitatively evaluate images and compare them across imaging devices. Such a truth does not exist in live subjects.

Computational phantoms are also widely used in imaging dosimetry. They can be used to estimate organ and effective dose from different examinations using Monte Carlo simulation techniques.[1–8] As such, computerized phantoms provide an effective tool to compare imaging applications in terms of dose as well as image quality. They also provide a means to prospectively estimate patient-specific organ and effective dose. With no practical technique to measure these values in patients, they are typically derived by matching a patient to a reference phantom for which the organ dose has been precalculated. The better the phantom matches the patient, the better the estimation of dose.

With their great potential, many different computerized phantoms are currently being developed for research. For these phantoms to be truly useful they must accurately model the human anatomy and physiology so simulations using them will be indicative of what would occur in live patients. The most realistic phantoms are typically based on the segmentation of patient imaging data, usually MRI or CT.[9] Beginning with the development of the nonuniform rational B-spline (NURBS)-based cardiac-torso (NCAT) phantom,[10,11] the latest work in phantom development has focused on the creation of hybrid models, phantoms based on the segmentation of imaging data but using surface representations such as NURBS or polygon meshes to define the structures. The surfaces realistically model the anatomy with the added bonus of greater flexibility to model anatomical variations and patient motion. To change the anatomy, one only has to apply transforms (rigid or nonrigid) to the surfaces.

The main bottleneck in creating such a phantom is the initial segmentation process. Segmentation of patient data is a time-consuming process that can take many months to a year to complete depending on the level of detail required. As a result, there is a barrier of sorts to creating vast populations of highly detailed models. In order to more closely mimic a clinical study or trial and to better estimate patient-specific dose, a large population of phantoms is needed to reflect the range of anatomical variations representative of the public at large. To overcome this barrier, many researchers have sought to produce anatomically variable populations of phantoms by altering their preexisting hybrid models,[12–16] making use of their great flexibility. To create new individuals, the template hybrid models are deformed to match statistical anthropometric measurements for given individuals. As a simple example, to create a larger patient from an existing one, the outer body surface can be scaled until it matches the measurements (chest, abdomen, and pelvis circumferences) typical for a person who is 90th percentile for height and weight. Based on statistics taken from autopsies, relationships have been derived for organ and tissue masses as a function of height.[17] These relationships can be used to scale organ volumes up and down to alter the interior of the new models. The main drawback to this method is that each new anatomy is ultimately derived from the template upon which it was originally based. Changes in organ shapes and positions from patient to patient are not captured.

Building upon our previous work with the NCAT phantom, we developed the 4D extended cardiac-torso (XCAT) phantom[18] for multimodality imaging research to evaluate and compare imaging devices and techniques. The 4D XCAT consists of whole-body adult male and female models which contain an unmatched level of detail and anatomical realism (Fig. 1). The male and female anatomies were originally based on the visible human anatomical imaging data, but were modified, through the phantom's flexibility, to match body measurements and organ volumes for a 50th percentile (height and weight) male and female. The male and female XCAT phantoms are extremely realistic, containing thousands of anatomical structures. Individual surfaces are defined for each muscle, bone, ligament, tendon, and blood vessel. An important innovation in the XCAT is its extension to 4D to model the cardiac and respiratory motions. Most hybrid phantoms are limited to 3D. The XCAT also includes parameterized models for the anatomy. Using these parameters, one can create an unlimited number of anatomical variations. As mentioned above, though, this population would still be limited, not truly capturing the interior variation from patient to patient.

In this work, we extended the original XCAT models to create a new adult population. Starting from clinical CT images, we applied a previously devised methodology[19] to efficiently morph the XCAT phantom to create 58 highly detailed, full-body 4D XCAT phantoms of varying body-mass-indices (BMIs). This method is similar to the previous studies mentioned above that transform template phantoms to create new ones. The main difference is that we use actual patient segmentations to guide our transforms. By doing this, we capture more of the interior variability from patient to patient. The result of this work is the first library of 4D computational phantoms.

II. MATERIALS AND METHODS

II.A. Patient selection and creation of initial models

The new XCAT models were constructed based on patient chest–abdomen–pelvis (CAP) CT datasets collected from the Duke University imaging database. Under approval of the Duke Institutional Review Board (IRB) and in compliance with the Health Insurance Portability and Accountability Act (HIPAA) regulations, we interrogated our Radiology Information System (RIS) to identify subjects for inclusion in the study. Patient cases were selected that exhibit normal anatomy such that if a disease was present, it did not manifest itself in any gross changes to internal organs in terms of size or location. As such, the variability in anatomy among the patient population was similar to that among a healthy population. CAP datasets were obtained to represent a wide range of

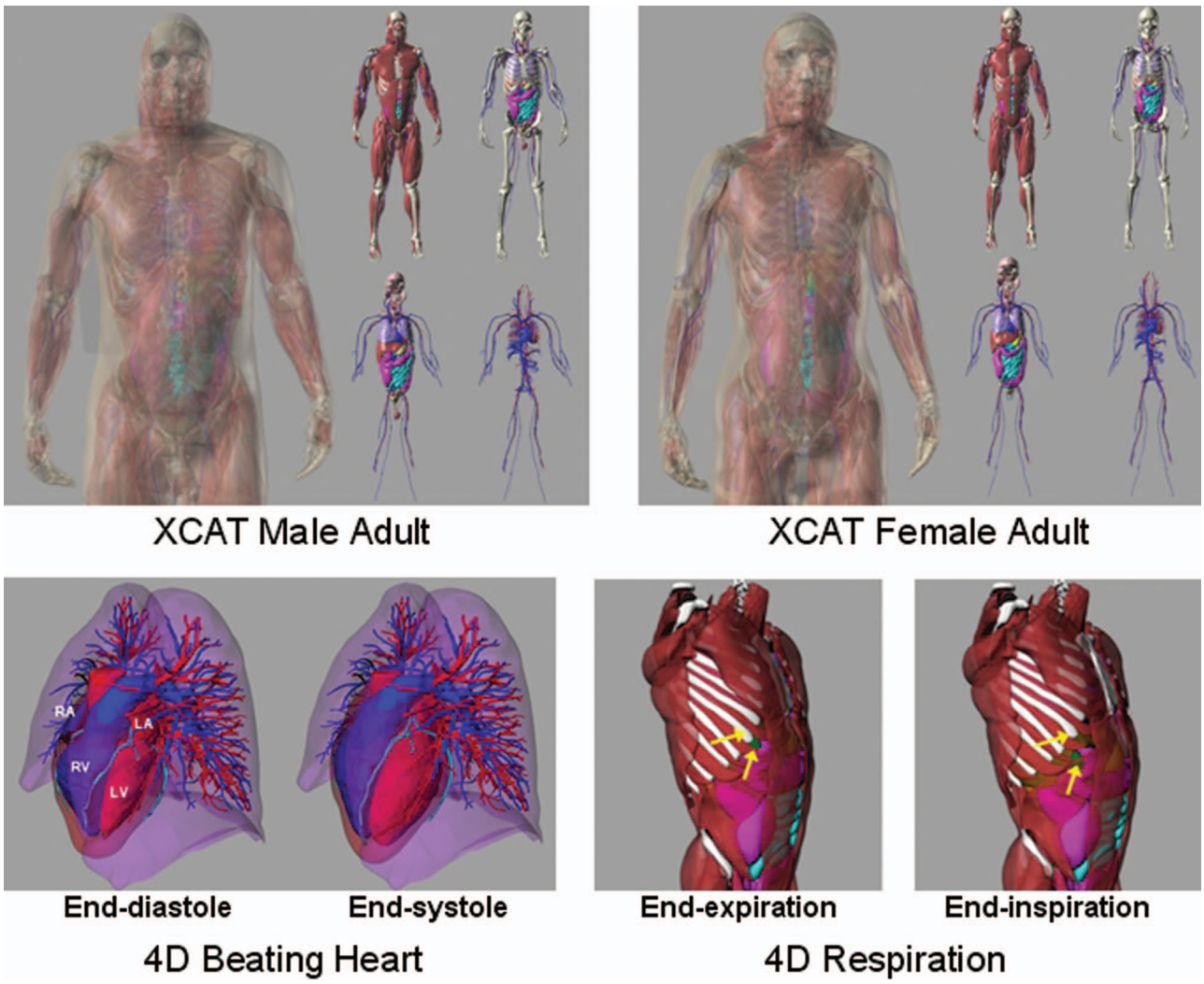

FIG. 1. (Top) 50th percentile male (left) and female (right) whole-body anatomies of the XCAT phantom. (Bottom) 4D cardiac and respiratory models of the XCAT.

body types for both adult males and females as determined by the BMI (Fig. 2). Thirty-five male (BMI from 19.2 to 36.1) and 23 female (BMI from 18.2 to 36.7) patient datasets were selected.

An initial patient model was created for each dataset using methods similar to those used to create the original XCAT male and female adult anatomies.[18] Selected organs and structures were manually segmented from each patient dataset using ImageSegment, an application developed in our laboratory. The structures segmented included the following: the body outline, the sternum, ribs, backbone, pelvis, scapulas, clavicles, left and right humerus, left and right femur, heart, lungs, liver, gall bladder, stomach, spleen, thyroid, kidneys, pancreas, intestines, prostate, and bladder. The testes were not segmented in the male patients due to the data not fully covering them. The humerus and femur for each arm and leg were not entirely visible in the CT data as well. Only the initial third of these bones was able to be segmented. These were used to guide the addition of template arm and leg models as detailed in Sec. II.B. The segmentations were performed by students using a cross-sectional anatomy book as a reference.[20] A tablet PC was used so that contours could be quickly and accurately drawn on the screen using a light pen. The segmentations were guided and verified by Dr. Paul Segars, who has a great deal of experience in segmenting imaging data in creating the NCAT and XCAT phantoms, and by Dr. Donald Frush, MD, Chief, Division of Pediatric Radiology at the Duke University Medical Center.

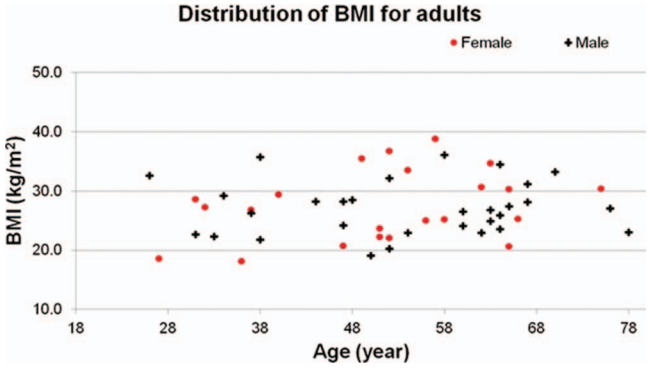

FIG. 2. BMI and ages of the patients used to develop the XCAT adult series.

The segmentation process produced a 3D mask image for each patient in which the individual organs were set to unique integer IDs or intensities. The different structures were converted into 3D polygon models using the marching cubes algorithm from the Visualization Toolkit (www.vtk.org) included in the ImageSegment software. The polygon models were imported into the Rhinoceros NURBS modeling software, www.rhino3d.com, and cubic NURBS surfaces were fit to them creating an initial NURBS-based patient model.

II.B. Extending the initial models to whole body

The initial model for each patient only covered the chest, abdomen, and pelvis region. To complete each phantom, we manually added on the head, arms, and legs using the existing male and female XCAT models as templates. The Rhinoceros modeling software was used to perform this task. Within Rhinoceros, we could move and scale the different structures as we needed. The XCAT head (male or female depending on patient gender), consisting of the outer skin surface, skull, and cervical vertebrae, was first added on to the patient model using the first thoracic vertebrae (T1) as a guide. The T1 of the XCAT head was centered onto the T1 model of the patient. The skin surface of the head was then scaled to match specific facial measurements (forehead circumference, neck circumference, nose width, and jaw width) determined for the particular patient based on their characteristics. The desired measurements were obtained using the PeopleSize program, http://www.openerg.com/psz/index.html, Fig. 3. PeopleSize contains 289 individual anthropometric dimensions categorized from 1st to the 99th percentile for children and adults in the US as well as other countries. Based on the patient's BMI, we determined what percentile they fall in for their particular age and gender. We then used PeopleSize to find the facial measurements for that percentile. We used statistics from US male and female adults to determine the measurements. Only the skin surface was scaled; the skull and vertebrae were not altered. We also used PeopleSize to determine arm and leg measurements (arm length, upper and lower arm skin circumferences, upper and lower leg skin circumferences) for the patient. The leg length was determined based on the recorded height of the patient. The height from the top of the head to the bottom of the pelvis was measured from the model. This distance was subtracted from the known patient height to determine the proper leg length. After scaling the limbs to match the body type of the patient, they were placed manually onto the rest of the anatomy within Rhinoceros using the segmented skeleton as a guide completing the initial whole-body model for the patient.

II.C. Application of the multichannel large deformation diffeomorphic metric mapping (MC-LDDMM) method to complete the models

Once the initial model was constructed for each patient, the MC-LDDMM algorithm, modified from its original use (working with diffusion tensor imaging data) to suit our application as described in Tward *et al.*,[19] was used to fill in the rest of the anatomy by transforming the selected template XCAT phantom (male or female) to match the framework defined for the target patient model.

This algorithm calculates a smooth invertible transformation (a diffeomorphism) φ, by minimizing the following

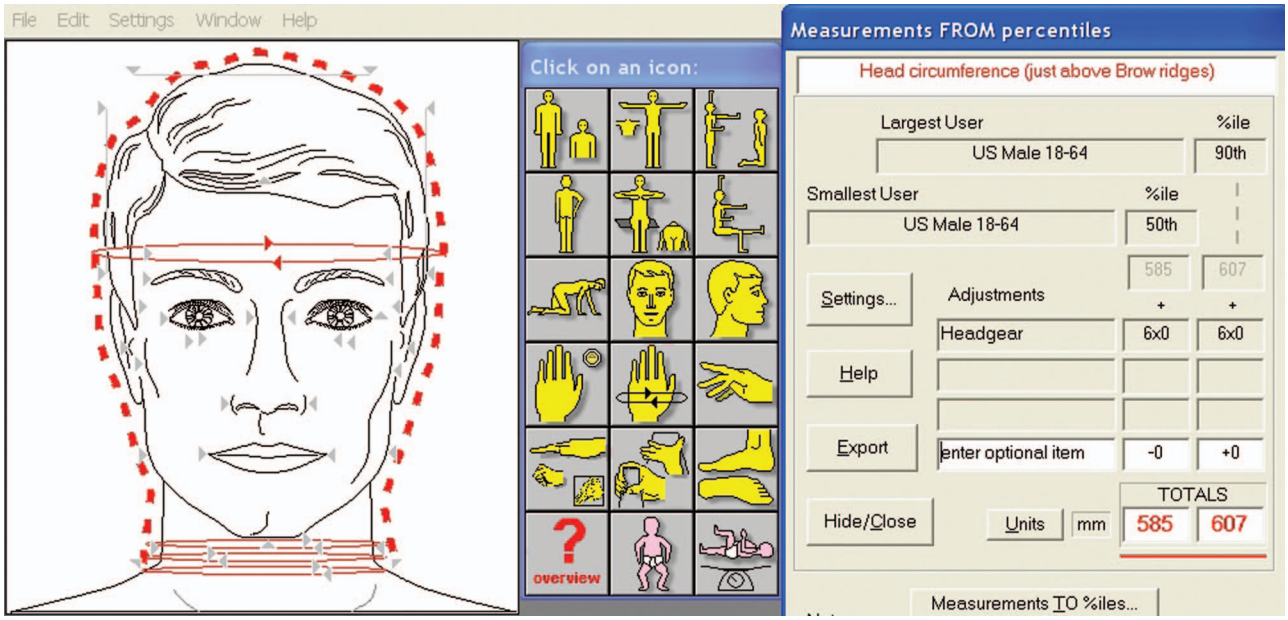

FIG. 3. Screenshot of the PeopleSize program. A user can select different regions of the body (middle menu) and display measurements for them at different percentiles (output on the right). The head is shown above as an example; the measurements for head circumference (50th and 90th percentile) are listed. A user can select the particular percentiles they want listed at the right in the program settings. They may also select the type of individuals they want. In this case, we selected US males, ages 18–64.

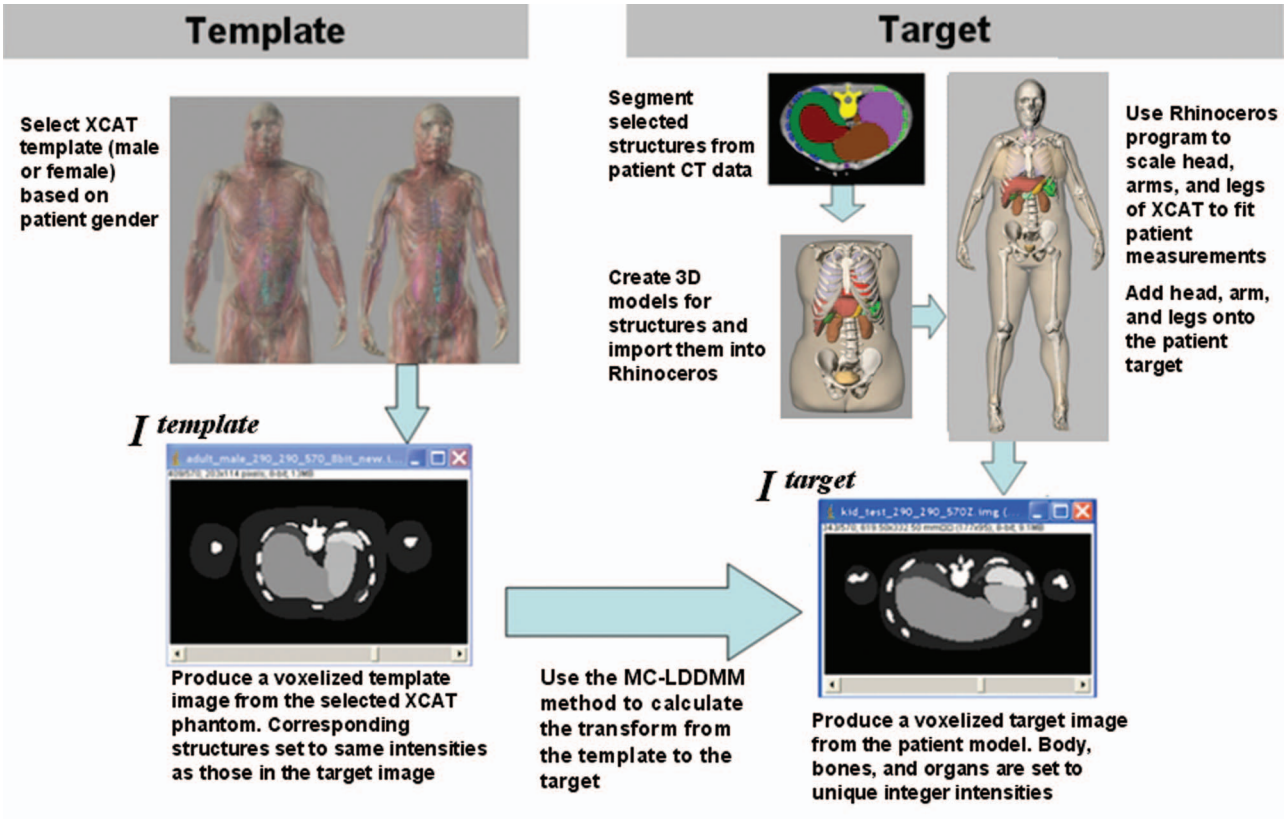

FIG. 4. Procedure for calculating the MC-LDDMM transform. To calculate the transform, template and target images are required. The above steps are performed to create these images. These images are further broken down into a binary image for each organ that is used to calculate the transform.

functional:

$$E = d(\varphi, Id)^2 + \sum_i \frac{1}{\sigma_i^2} \| I_i^{\text{template}} o\varphi^{-1} - I_i^{\text{target}} \|_{\text{L2}}^2, \quad (1)$$

where $d(\varphi, Id)$ is the distance between φ and the identity transformation on the diffeomorphism group,[21] $\| \cdot \|_{\text{L2}}^2$ denotes the L2 norm squared (integral over the square of a function), σ_i^2 denotes a weighting factor for each organ, and I_i^{template} and I_i^{target} represent binary images describing the ith organ in the limited framework. These binary images of the XCAT template and the patient target for each case were created by voxelizing the template and target models into 3D images (isotropic resolution of 2 mm) covering the whole body. The template model was set to contain the same structures as the target.

To increase robustness which can be a challenge for high dimensional mappings in heterogeneous populations, labeled landmarks were defined using the template and target skeletons. Corresponding landmarks were placed on the endpoints of bones such as the ribs, arm/leg bones, and sternum. The spinal processes also served as landmarks. The landmarks were used to calculate initial low dimensional transformations (an affine transformation, followed by a landmark based nonlinear transformation[22]) before attempting to minimize the functional above. It took approximately 6–8 h to calculate each transform. Figure 4 summarizes the steps to calculate the MC-LDDMM transform. The images shown in the figure, I^{template} and I^{target} are broken down into a binary image for each organ i to calculate the transform. They are shown in the figure as single images for display purposes.

Since φ is defined as a diffeomorphism on the background space, rather than as a displacement of organ boundaries, it can be applied to the template XCAT to create a new XCAT phantom for a patient containing all anatomical structures (Fig. 5), even those missing from the limited framework. The MC-LDDMM algorithm guarantees that the transformation is a diffeomorphism, allowing image and surface data to be mapped between template and target while preserving topology and smoothness. Even with a small number of segmented organs defined, the optimal φ will interpolate smoothly through the background space, allowing missing organs to be deformed with a high accuracy as demonstrated previously.[23] For this work, we segment the major structures to make the transform as accurate as possible; Table I lists the structures that are segmented and the structures that are predicted using the MC-LDDMM transform. The MC-LDDMM method has proven to provide accurate transforms for identified objects.[19] As shown in our study,[23] the predicted anatomy will also provide a good match for what we segment. For our purposes, we do not need a perfect transform since our goal is not to generate patient specific models that perfectly match given subjects. This would not be achievable since we do not have whole-body data to work from. We are already varying

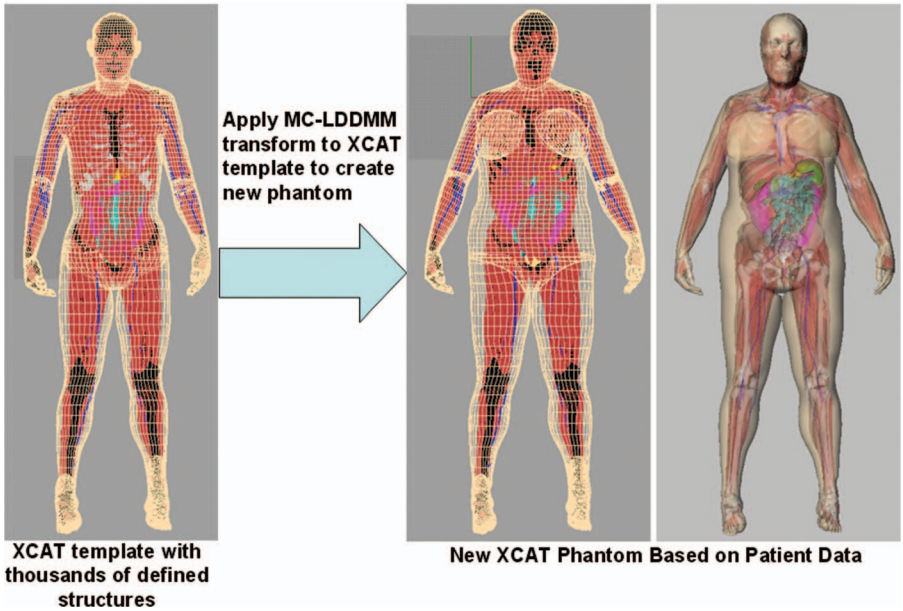

FIG. 5. The MC-LDDMM transform is used to transform the template XCAT phantom to define the detailed anatomy of the target phantom. The new XCAT model, based on the patient data, contains the same structures as the original XCAT.

from the patient by adding on the head, arms, and legs from template models. Our goal is to generate several anatomically variable models that can be used for imaging research similar to what others have done in modifying their hybrid phantoms. We just use a high order nonrigid registration to transform our templates and guide this transform using the segmented patient anatomy. We feel this method captures more interior variation from subject to subject.

II.D. Incorporation of cardiac and respiratory motions

To make the phantoms applicable to dynamic imaging research, we incorporated cardiac and respiratory models into each creating a 4D model. This required little effort as the underlying cardiac and respiratory models already exist in the template XCAT phantom. The MC-LDDMM transform was applied to the base 4D cardiac model of the XCAT to implement it in the new anatomy. The respiratory motion was modeled in each new phantom based on similar mechanics to that of the original XCAT.[18] The ribcage rotates upward and outward expanding the chest during inspiration and the diaphragm contracts downward and forward. The heart, liver, stomach, spleen, kidneys, and abdominal organs move with scaled down motions from that of the diaphragm. Both cardiac and respiratory models were parameterized as in the original XCAT adult models.

II.E. Fine tuning of the models

Finally, each new phantom was refined by checking for anatomical accuracy via visual inspection of the 3D models and comparison of the volumes for predicted structures to those from ICRP Publication 89 (Ref. 24) and values predicted for a particular individual based on their height.[17] If needed, minor adjustments were made by scaling undersized or oversized organs. Like the original XCAT, the new phantoms were setup with parameters to adjust the organs (see Table 2 from Ref. 18). The weight for each phantom was also calculated and compared to the patient weight from their record. Each phantom was voxelized to a very fine resolution (1 mm isotropic), and the voxels for the different tissues were counted then multiplied by the density of the material. The densities used in this calculation can be found at http://physics.nist.gov/PhysRefData/XrayMassCoef/tab2.html. The phantom weights were found to generally agree with the actual patient weights; the maximum error was less than 10%. Despite this, the weights of the phantoms were finely adjusted to match the patient weight within 1%. This was done by scaling the skin surfaces of the arms and legs. These structures were add-ons, not based on the actual imaging data, and carry a good deal of weight so they provided the best means for the adjustment. Each new XCAT phantom was setup with parameters to perform this scaling, adjusting the muscles, tendons, ligaments, and vessels inside the arms and legs while keeping the bones constant. Using these methods, 4D phantoms of multiple body types and sizes were created to match the height and weight of different patients.

III. RESULTS

We created a new population of 58 (35 male and 23 female) anatomically variable adult XCAT phantoms for imaging research. Figure 6 shows a collage of the phantoms, illustrating the changing interior anatomy in the region covered by the imaging data. With the MC-LDDMM method, it was

TABLE I. List of structures in the new XCAT phantoms that are obtained using the template models, through segmentation, or by using the MC-LDDMM transform.

Obtained from XCAT template head, arms and legs	Segmented in the CT data	Predicted with MC-LDDMM
Head (skin)	Body (skin)	Adrenals
Skull	Breasts	Arteries and veins in the body
Eyes	Thyroid	Muscle, ligaments, and tendons in the body
Oral cavity	Pericardium[a]	Esophagus
Tonsils	Lungs	Larynx
Tongue	Liver	Pharynx
Salivary glands	Gall bladder	Thymus
Mandible	Stomach	Heart and its interior structures[a]
Teeth	Spleen	Ovaries
Brain and its interior structures	Pancreas	Fallopian tubes
Muscles, arteries, veins, ligaments, and tendons in the head	Kidneys	Uterus
Arms and legs (skin)	Intestines	Vagina
Muscles, arteries, veins, ligaments, and tendons in the arms and legs	Bladder	Trachea and bronchi
Humerus[b]	Prostate	Penis
Radius	Sternum	Ejaculatory ducts
Ulna	Ribs	Epididymis
Bones in hand and fingers	Vertebrae	Seminal vesicles
Femur[b]	Pelvis	Testes
Tibia	Sacrum	Vas deferens
Fibula	Scapula	Ureter
Patella	Clavicle	Urethra
Bones in foot and toes	Humerus[b]	
	Femur[b]	

[a]Pericardial surface is segmented to guide the heart transform.
[b]Humeri and femurs are partially segmented in the CT data and used to help place the template arm bones.

possible to efficiently create whole body phantoms with many anatomical structures, some not easily visible in the original CT data. Figure 7 shows the results of mapping the male XCAT anatomy to a large male patient (BMI = 36). Since the new phantoms were formed by transforming the original XCAT models, each contained the same amount of detail and structures as the original XCAT (see Table 4 from Ref. 18). Each phantom includes all the radiosensitive organs (organs with tissue weighting factors in dose calculations) as well as many other structures. The high level of detail is important so that the phantoms are applicable to high-resolution imaging applications such as CT and MRI. Without modeling small details, the imaging data simulated from the phantoms would not be close to what you would see from live patients, limiting their use. Ultimately, we would like to apply the phantoms to image quality versus dose studies. To simulate realistic images for this purpose requires a great deal of detail. The new phantoms also maintained the same features and flexibility of the XCAT, each containing parameterized models for the anatomy and the cardiac and respiratory motions (see Table 2 from Ref. 18) and can, therefore, serve as a jumping point from which to further create 3D and 4D variations for imaging research.

Like the XCAT, the new series of phantoms can be combined with simulation packages (PET, SPECT, CT, MRI, ultrasound) to generate realistic imaging data. Many excellent, publicly available simulation packages in SPECT/PET,[25,26] MRI,[27–29] CT,[30–32] and ultrasound[33,34] have been developed and validated that can be used with the phantoms. Figure 8 shows simulated CT data from four anatomically variable males and females as a demonstration. The data were generated using an analytical CT simulator developed in our laboratory.[35] The CT data look very realistic, but are hampered by the fact that each structure has a uniform attenuation characteristic. We plan to investigate techniques to model interior heterogeneous organ textures within the phantoms to improve the realism.

With the new series of XCAT models, we now have multiple body types and sizes allowing for patient variability common of a clinical trial. Table II shows the mean organ masses and standard deviations from the population as compared to the standard volumes for the adult male and female from ICRP 89. As can be seen in the table, there is a great deal of variation in the organ masses (for those organs defined by CT segmentation). The mass of the breasts was found to differ the most from the ICRP values. The breasts were difficult to segment in that it was hard to determine where they end and the chest wall begins. It is possible that there is some over segmentation included in the calculated volumes. Despite that, we did find a great deal of variation in the breast masses, ranging from 300 to 3000 g. The mean stomach mass also differed with the ICRP values, but this can be expected given the stomach volume changes a great deal depending on how much the subject ate prior to imaging. The masses for the pancreas, spleen, and gallbladder were also found to vary from the ICRP values; however, their masses did fall into the range observed in other studies.[17,36,37]

IV. DISCUSSION

In this work, we created the first library of 4D computational phantoms. The MC-LDDMM method provided a novel and highly efficient tool, allowing the rapid development of realistic anatomically diverse 4D computational models by morphing an anatomical template. Using our techniques, it was possible to create a new patient model, containing all structures defined in the XCAT, within 3-4 days. Like most phantom development, the major bottleneck in the process was the creation of the initial patient model using segmentation. The MC-LDDMM calculation itself only took about 6–8 h per model. In this work, we segmented a great deal of structures to ensure accurate transforms. We

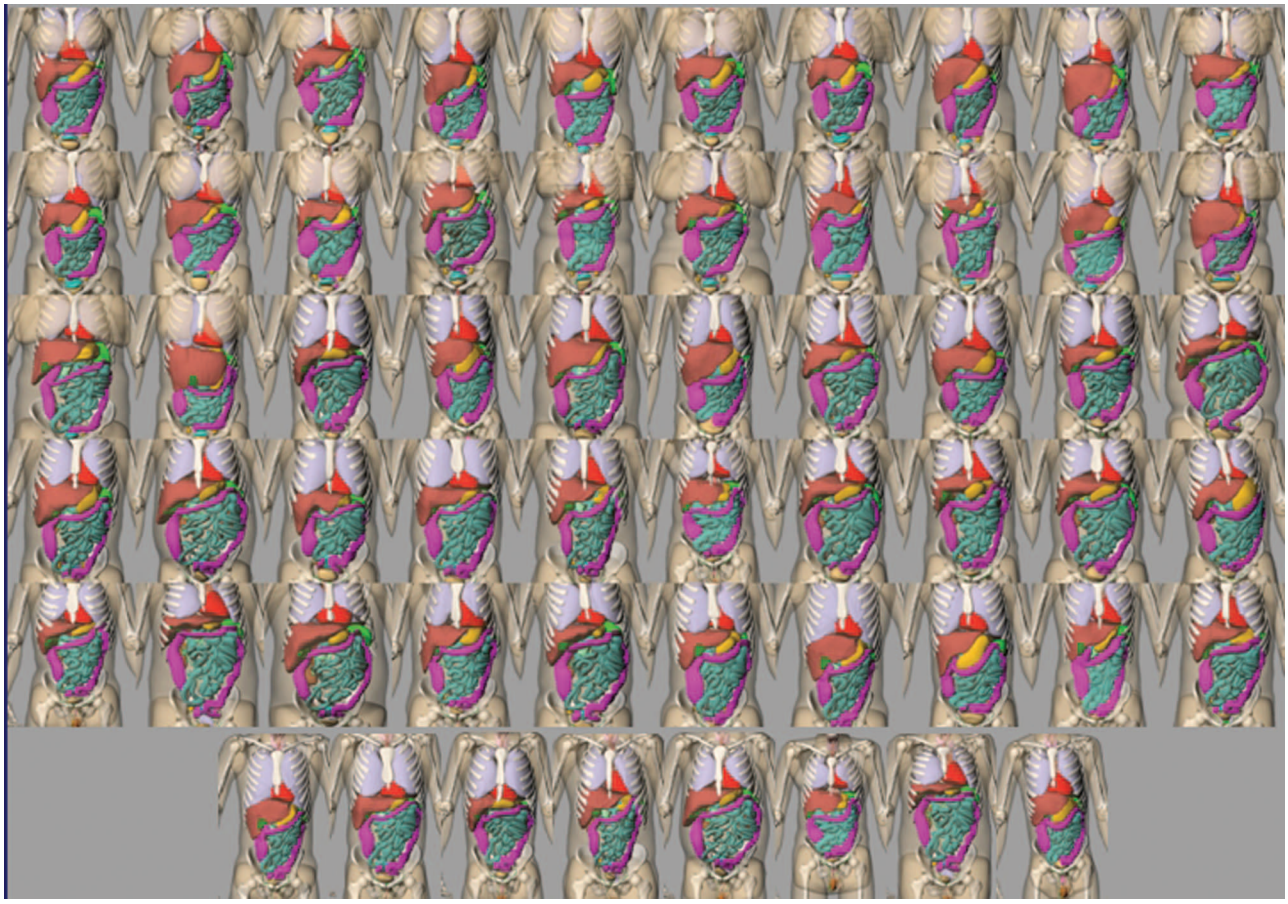

FIG. 6. Collage showing the 58 new adult anatomies. The head, arms, and legs are not shown to focus on the chest–abdomen–pelvis anatomy, which is based on the patient imaging data. The muscles and blood vessels are also not shown for presentation purposes.

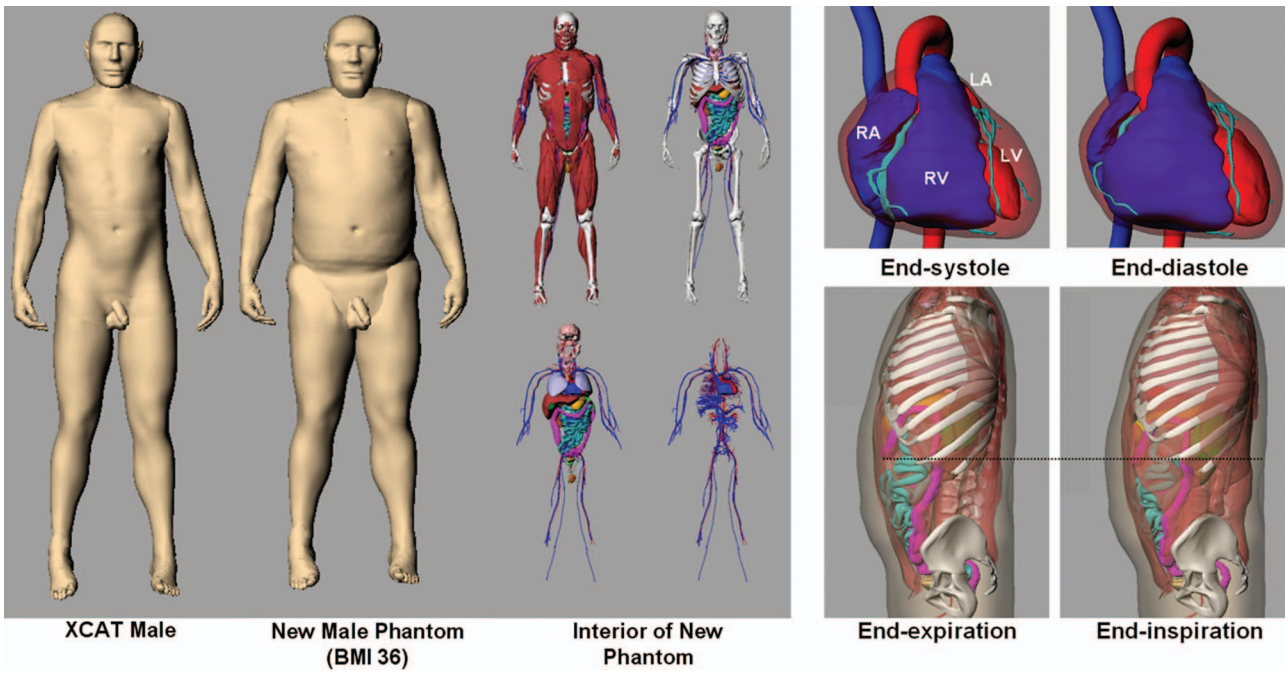

FIG. 7. New male phantom (BMI = 36) created by transforming the original male XCAT. The original XCAT is shown to the left while the new phantom is shown in the middle. The interior anatomy of the male phantom is shown with varying levels of detail. The new phantom contains the same number of structures as the original XCAT. The phantom also includes the models for the cardiac and respiratory motions. The new phantom is shown to the right at different phases of the cardiac and respiratory cycles. The dotted line in the respiratory pictures shows how the internal organs are moving.

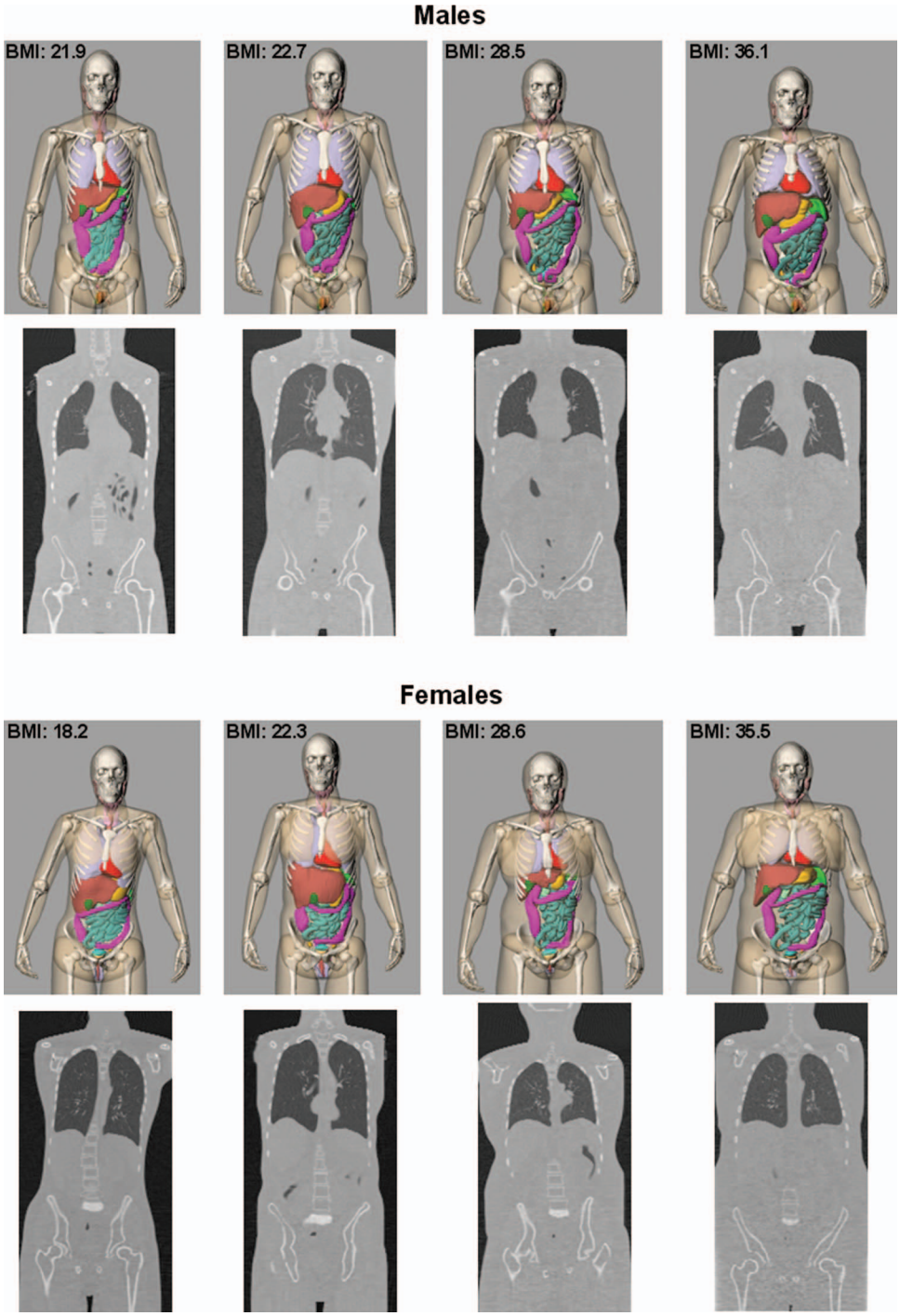

FIG. 8. Four adult male (top) and four adult female (bottom) XCAT phantoms with CT simulation results shown at the bottom.

plan to investigate optimizing the segmentation part of the process so new models can be created within hours. We will look into what structures are necessary to segment in order to maintain an accurate transform from the template to the target.

The techniques used to create our phantoms are similar to those used previously to create new models by transforming existing templates.[12–16] By using segmented patient imaging data to guide our transforms, though, we capture more of the interior variability in the organ shapes and positions from patient to patient. Our models are also very highly detailed and 4D making them applicable to high-resolution 3D and 4D imaging studies. A drawback to these models is that the head, arms, and legs are still created by adding on scaled template versions. We plan to use PET-CT data in the future to develop more phantoms; the particular data we plan to use cover the head and will give us more variability in that area.

TABLE II. Mean and standard deviation of the organ masses of the adult models as compared with the organ masses from ICRP 89.

	Mean organ mass (g)		ICRP 89 organ mass (g)		Percent difference	
	Male (%)	Female (%)	Male	Female	Male (%)	Female (%)
Prostate	18.1 ± 13		17		6	
Testes	32.3 ± 5		35		−8	
Breasts		1249.0 ± 51		500		150
Ovaries		11.1 ± 5		11		1
Uterus		83.7 ± 4		80		5
Brain	1497.9 ± 2	1364.4 ± 1	1450	1300	3	5
Lungs[a]	1310.2 ± 23	1036.5 ± 22	1200	950	9	9
Liver	1871.5 ± 24	1567.4 ± 18	1800	1400	4	12
Pancreas	106.3 ± 34	74.8 ± 42	140	120	−24	−38
Stomach[b]	303.1 ± 47	217.9 ± 54	400	370	−24	−41
Esophagus[c]	40.1 ± 5	35.1 ± 5	40	35	0	0
Larynx/pharynx	31.2 ± 10	21.9 ± 7	26	19	11	15
Spleen	240.4 ± 39	169.7 ± 38	150	130	60	31
Gallbladder	33.3 ± 58	25.1 ± 80	68	56	−51	−55
Kidneys	363.5 ± 26	298.1 ± 18	310	275	17	8
Adrenals	14.9 ± 7	13.5 ± 13	14	13	6	4
Small intestine[b]	1025.8 ± 5	842.8 ± 15	1000	830	3	−4
Large intestine[b]	704.7 ± 3	690.8 ± 11	670	680	5	2
Bladder[c]	50.5 ± 5	40.5 ± 5	50	40	1	1
Thyroid	21.9 ± 5	18.6 ± 1	20	17	9	9
Thymus	24.4 ± 7	19.3 ± 4	25	20	−2	−3
Salivary glands	90.8 ± 3	75.3 ± 3	85	70	7	8
Pituitary	0.6 ± 0	0.6 ± 1	0.6	0.6	5	5
Eyes	15.2 ± 1	15.5 ± 3	15	15	1	3
Trachea[c]	10.1 ± 5	8.1 ± 5	10	8	1	1
Heart[a]	810.3 ± 20	668.6 ± 20	840	620	−4	8
Muscle, skeletal	29 929 ± 13	20 465 ± 8	29 000	17 500	3	17
Skeleton, total	10 351 ± 10	8821.7 ± 5	10 500	7800	−1	13
Marrow[d]	3598 ± 10	3053 ± 5	3650	2700	−1	13
Total body (kg)	85.4 ± 19	73.9 ± 19	73	60	17	23

[a]Mass with blood.
[b]Mass of wall and contents.
[c]Based on enclosed volume of hollow structure, where the wall thickness can be defined in the phantom program.
[d]Bone marrow determined as fractional distribution of total skeleton. Alternatively, bone thickness can be specified by the user to define the amount of marrow contained within the bones.

V. CONCLUSION

With the rise of computer simulation in imaging research, a population of phantoms that includes a range of anatomical variations representative of the public at large is needed to more closely mimic a clinical study or trial. The series of anatomically variable phantoms developed in this work provide a valuable resource for investigating different imaging devices and the effects of anatomy and motion in imaging. With recent advances toward more volumetric and dynamic imaging, the phantoms have enormous potential to study the effects of anatomical, physiological, physical, and instrumentational factors on imaging and to research new image acquisition strategies, image processing and reconstruction methods, and image visualization and interpretation techniques. Combined with accurate models for the imaging process, the phantoms can provide a wealth of realistic, predictive imaging data of a patient population to serve as a known truth from which to evaluate and improve 3D and 4D imaging techniques used for the diagnosis and treatment of disease. Such simulated imaging data also have great potential to be used in medical education as a training tool for physicians. It can be used to simulate any number of different situations using various imaging applications (CT, MRI, ultrasound, SPECT, PET) and scanning parameters (spatial and temporal resolution, dose, kVp, radiopharmaceutical, etc.).

Combined with accurate Monte Carlo dose estimation programs, the phantom series will also provide the necessary foundation to optimize imaging applications in terms of image quality and radiation dose and to enable patient-specific estimation of dose and radiation risk. With a library of anatomies to choose from, better matches may be found for a particular patient that would enable more accurate prospective estimation of patient-specific organ and effective dose. We have already used the phantoms to study the effects of protocol and obesity on dose conversion factors in body CT[38] and to study organ doses, effective doses, and risk indices across a selected group of representative CT protocols.[39] We are

currently using them to compare dosimetry in chest radiography, CT, and tomosynthesis.

In future work, we plan to further expand this library, ultimately to a population of hundreds of phantoms ranging in age from newborn to adult. Such a large compilation of phantoms will provide a great research tool for the imaging community.

ACKNOWLEDGMENTS

This work was supported by the research Grant No. R01 EB001838 from the National Institutes of Health.

[a]Author to whom correspondence should be addressed. Electronic mail: paul.segars@duke.edu; Telephone: 919-684-1473.

[1]M. Zankl, W. Panzer, N. Petoussihenss, and G. Drexler, "Organ doses for children from computed tomographic examinations," Radiat. Prot. Dosim. **57**(1–4), 393–396 (1995).

[2]M. Caon, G. Bibbo, and J. Pattison, "An EGS4-ready tomographic computational model of a 14-year-old female torso for calculating organ doses from CT examinations," Phys. Med. Biol. **44**(9), 2213–2225 (1999).

[3]M. Caon, G. Bibbo, and J. Pattison, "Monte Carlo calculated effective dose to teenage girls from computed tomography examinations," Radiat. Prot. Dosim. **90**(4), 445–448 (2000).

[4]N. Karabulut, M. Toru, V. Gelebek, M. Gulsun, and O. M. Ariyurek, "Comparison of low-dose and standard-dose helical CT in the evaluation of pulmonary nodules," Eur. Radiol. **12**(11), 2764–2769 (2002).

[5]I. A. Castellano, D. R. Dance, and P. M. Evans, "CT dosimetry: Getting the best from the adult cristy phantom," Radiat. Prot. Dosim. **114**(1–3), 321–325 (2005).

[6]J. J. DeMarco, C. H. Cagnon, D. D. Cody, D. M. Stevens, C. H. McCollough, M. Zankl, E. Angel, and M. F, McNitt-Gray, "Estimating radiation doses from multidetector CT using Monte Carlo simulations: Effects of different size voxelized patient models on magnitudes of organ and effective dose," Phys. Med. Biol. **52**(9), 2583–2597 (2007).

[7]C. Lee, R. J. Staton, D. E. Hintenlang, M. M. Arreola, J. L. Williams, and W. E. Bolch, "Organ and effective doses in pediatric patients undergoing helical multislice computed tomography examination," Med. Phys. **34**(5), 1858–1873 (2007).

[8]C. Lee, D. Lodwick, J. L. Williams, and W. E. Bolch, "Hybrid computational phantoms of the 15-year male and female adolescent: Applications to CT organ dosimetry for patients of variable morphometry," Med. Phys. **35**(6), 2366–2382 (2008).

[9]M. Caon, "Voxel-based computational models of real human anatomy: A review," Radiat. Environ. Biophys. **42**, 229–235 (2004).

[10]W. P. Segars, D. S. Lalush, and B. M. W. Tsui, "A realistic spline-based dynamic heart phantom," IEEE Trans. Nucl. Sci. **46**, 503–506 (1999).

[11]W. P. Segars, "Development of a new dynamic NURBS-based cardiac-torso (NCAT) phantom," Ph.D. dissertation, The University of North Carolina, 2001.

[12]A. Ding, M. M. Mille, T. Liu, P. F. Caracappa, and X. G. Xu, "Extension of RPI-adult male and female computational phantoms to obese patients and a Monte Carlo study of the effect on CT imaging dose," Phys. Med. Biol. **57**(9), 2441–2459 (2012).

[13]P. B. Johnson, S. R. Whalen, M. Wayson, B. Juneja, C. Lee, and W. E. Bolch, "Hybrid patient-dependent phantoms covering statistical distributions of body morphometry in the US adult and pediatric population," Proc. IEEE **97**(12), 2060–2075 (2009).

[14]Y. H. Na, B. Zhang, J. Zhang, P. F. Caracappa, and X. G. Xu, "Deformable adult human phantoms for radiation protection dosimetry: Anthropometric data representing size distributions of adult worker populations and software algorithms," Phys. Med. Biol. **55**(13), 3789–3811 (2010).

[15]V. F. Cassola, F. M. Milian, R. Kramer, C. A. B. de Oliveira Lira, and H. J. Khoury, "Standing adult human phantoms based on 10th, 50th and 90th mass and height percentiles of male and female Caucasian populations," Phys. Med. Biol. **56**(13), 3749–3772 (2011).

[16]D. Broggio, J. Beurrier, M. Bremaud, A. Desbree, J. Farah, C. Huet, and D. Franck, "Construction of an extended library of adult male 3D models: Rationale and results," Phys. Med. Biol. **56**(23), 7659–7692 (2011).

[17]G. L. de la Grandmaison, I. Clairand, and M. Durigon, "Organ weight in 684 adult autopsies: New tables for a Caucasoid population," Forensic Sci. Int. **119**(2), 149–154 (2001).

[18]W. P. Segars, S. Mendonca, J. Grimes, G. Sturgeon, and B. M. W. Tsui, "4D XCAT phantom for multimodality imaging research," Med. Phys. **37**, 4902–4915 (2010).

[19]D. J. Tward, C. Ceritoglu, A. Kolasny, G. M. Sturgeon, W. P. Segars, M. I. Miller, and J. T. Ratnanather, "Patient specific dosimetry phantoms using multichannel LDDMM of the whole body," Int. J. Biomed. Imaging (2011).

[20]P. Fleckenstein and J. Tranum-Jensen, *Anatomy in Diagnostic Imaging* (W. B Saunders, Denmark, 1996).

[21]M. I. Miller, A. Trouve, and L. Younes, "On the metrics and Euler-Lagrange equations of computational anatomy," Annu. Rev. Biomed. Eng. **4**, 375–405 (2002).

[22]S. C. Joshi and M. I. Miller, "Landmark matching via large deformation diffeomorphisms," IEEE Trans. Image Process. **9**(8), 1357–1370 (2000).

[23]W. P. Segars, G. Sturgeon, X. Li, L. Cheng, C. Ceritoglu, J. T. Ratnanather, M. I. Miller, B. M. W. Tsui, D. Frush, and E. Samei, "Patient specific computerized phantoms to estimate dose in pediatric CT," Proc. SPIE **7258**, 72580H–72580H-9 (2009).

[24]B. Axelsson, J. Persliden, and P. Schuwert, "Dosimetry for computed tomography examination of children," Radiat. Prot. Dosim. **64**, 221–226 (1996).

[25]I. Buvat and D. Lazaro, "Monte Carlo simulations in emission tomography and GATE: An overview," Nucl. Instrum. Methods Phys. Res. A **569**(2), 323–329 (2006).

[26]H. Zaidi, "Relevance of accurate Monte Carlo modeling in nuclear medical imaging," Med. Phys. **26**(4), 574–608 (1999).

[27]T. H. Jochimsen, A. Schafer, R. Bammer, and M. E. Moseley, "Efficient simulation of magnetic resonance imaging with Bloch-Torrey equations using intra-voxel magnetization gradients," J. Magn. Reson. **180**(1), 29–38 (2006).

[28]H. Benoit-Cattin, G. Collewet, B. Belaroussi, H. Saint-Jalmes, and C. Odet, "The SIMRI project: A versatile and interactive MRI simulator," J. Magn. Reson. Imaging **173**(1), 97–115 (2005).

[29]D. A. Yoder, Y. S. Zhao, C. B. Paschal, and J. M. Fitzpatrick, "MRI simulator with object-specific field map calculations," Magn. Reson. Imaging **22**(3), 315–328 (2004).

[30]J. M. Boone, M. H. Buonocore, and V. N. Cooper, "Monte Carlo validation in diagnostic radiological imaging," Med. Phys. **27**(6), 1294–1304 (2000).

[31]X. Li, E. Samei, W. P. Segars, G. M. Sturgeon, J. G. Colsher, G. Toncheva, T. T. Yoshizumi, and D. P. Frush, "Patient-specific radiation dose and cancer risk estimation in CT: Part I. Development and validation of a Monte Carlo program," Med. Phys. **38**(1), 397–407 (2011).

[32]A. Malusek, M. Sandborg, and G. A. Carlsson, "CTmod—A toolkit for Monte Carlo simulation of projections including scatter in computed tomography," Comput. Methods Programs Biomed. **90**(2), 167–178 (2008).

[33]H. Gao, H. F. Choi, P. Claus, S. Boonen, S. Jaecques, G. H. van Lenthe, G. Van der Perre, W. Lauriks, and J. D'Hooge, "A fast convolution-based methodology to simulate 2-D/3-D cardiac ultrasound images," IEEE Trans. Ultrason. Ferroelectr. Freq. Control **56**(2), 404–409 (2009).

[34]J. A. Jensen, "Ultrasound imaging and its modeling," Imaging Complex Media Acoust. Seism. Waves **84**, 135–165 (2002).

[35]W. P. Segars, M. Mahesh, T. J. Beck, E. C. Frey, and B. M. W. Tsui, "Realistic CT simulation using the 4D XCAT phantom," Med. Phys. **35**(8), 3800–3808 (2008).

[36]S. M. A. Kishk, R. M. A. Darweesh, W. J. Dodds, T. L. Lawson, E. T. Stewart, M. K. Kern, and E. H. Hassanein, "Sonographic evaluation of resting gallbladder volume and postprandial emptying in patients with gallstones," Am. J. Roentgenol. **148**(5), 875–879 (1987).

[37]D. C. Chan, T. M. Chang, C. J. Chen, T. W. Chen, J. C. Yu, and Y. C. Liu, "Gallbladder contractility and volume characteristics in gallstone dyspepsia," World J. Gastroenterol. **10**(5), 721–724 (2004).

[38]X. Li, E. Samei, C. H. Williams, W. P. Segars, D. J. Tward, M. I. Miller, J. T. Ratnanather, E. K. Paulson, and D. Frush, "Effects of protocol and obesity on dose conversion factors in adult body CT," Med. Phys. **39**(11), 6550–6571 (2012).

[39]Y. K. Zhang, X. Li, W. P. Segars, and E. Samei, "Organ doses, effective doses, and risk indices in adult CT: Comparison of four types of reference phantoms across different examination protocols," Med. Phys. **39**(6), 3404–3423 (2012).